





**Oblique magnetic anisotropy and domain texture in  $\text{Bi}_3\text{Fe}_5\text{O}_{12}$  films**Kishori Lal , Ravinder Kumar ,\* Pramod Ghising,<sup>†</sup> B. Samantaray , and Z. Hossain<sup>‡</sup>  
*Department of Physics, Indian Institute of Technology, Kanpur 208016, India* (Received 5 September 2022; revised 26 April 2023; accepted 6 June 2023; published 5 July 2023)

Magnetic iron garnet films with perpendicular magnetic anisotropy (PMA) are highly desirable for spintronics and magnonics applications. In this study, we have grown single-phase epitaxial  $\text{Bi}_3\text{Fe}_5\text{O}_{12}$  films on a  $\text{Gd}_3\text{Ga}_5\text{O}_{12}$  substrate with (111) orientation. The nondestructive  $\sin^2\psi$  technique of the x-ray diffraction measurement demonstrates the negative value of residual stress, suggesting the compressive nature of stress in the system. Ferromagnetic resonance and magnetic force microscopy (MFM) have been used to probe the magnetic anisotropies and magnetic domain texture, respectively. In-plane (IP) angular variation of the resonance field  $H_r$  reveals a weak IP magnetic anisotropy with pronounced sixfold and fourfold symmetries in 15 and 10 nm thick films, respectively. For the 15 nm thick film, the out-of-plane angular variation of  $H_r$  shows oblique magnetic anisotropy with the magnetic easy axis making an angle of  $25^\circ$  with respect to the film plane. The oblique magnetic easy axis is further confirmed with  $\theta$  mapping of the MFM image. However, for the 10 nm thick film there is complete reorientation of the magnetic easy axis perpendicular to the film plane. The cubic magnetocrystalline anisotropy along with the magnetoelastic anisotropy overcomes the shape anisotropy and leads to negative effective magnetic anisotropy  $K_{\text{eff}}$  and PMA. MFM images show a labyrinthine maze-like domain texture, typical of iron garnet films with PMA.

DOI: [10.1103/PhysRevB.108.014401](https://doi.org/10.1103/PhysRevB.108.014401)**I. INTRODUCTION**

Among the magnetic iron garnets, yttrium iron garnet (YIG) possesses low Gilbert damping ( $\sim 10^{-5}$ ) [1], a narrow linewidth in ferromagnetic resonance (FMR) spectra [2], interfacial phenomena [3,4], and substantial Faraday rotation [5]. These properties make YIG an ideal material for application in microwave and magneto-optical devices. Iron garnet films with perpendicular magnetic anisotropy (PMA) are desirable because they provide a platform to investigate various interesting phenomena such as spin-orbit torque [6], chiral magnetic texture [7–9], and spin pumping [10,11]. Along with this, they offer higher thermal stability, higher storage density, and lower power consumption, which eventually makes them suitable for data storage devices. However, YIG thin films, the most common among rare earth iron garnets (REIGs) show an in-plane (IP) magnetic easy axis due to the large shape anisotropy and low magnetocrystalline anisotropy [12]. In order to surpass the shape anisotropy and increase PMA in garnet films, one can introduce growth and stress-induced anisotropy. Since developing PMA in high-quality YIG films on  $\text{Gd}_3\text{Ga}_5\text{O}_{12}$  (GGG) substrates is challenging, the yttrium site in YIG has been substituted by various rare earth ions,

including Tm, Tb, Dy, Ho, Sm, Eu [13], Ce [14], and Bi [15], to explore the possibility of achieving PMA and tuning its magnetic properties.

It is well established that partial or complete substitution of the Y site with Bi and Ce ions enhances the magneto-optical activity, magnetocrystalline anisotropy, and magnetoelastic coupling in YIG [16,17]. Ce-doped YIG films have been studied for their magnetic texture (stripe domains) using magnetic force microscopy (MFM) [18] and Bi-doped YIG to tune magnetocrystalline anisotropy [17]. The magnetic texture and magnetization dynamics of Bi-doped YIG still require further investigation of their application in heterostructures, magnetic memory, and magneto-optical and thermomagnetic recording devices. Previous reports on Bi-doped YIG (BIG) films grown on GGG(001) investigated their magnetic, magneto-optical, and magnetoelectric properties [19–21]. However, in all of these studies, the magnetic easy axis lies in the film plane down to a film thickness of 5 nm. We have been able to achieve an out-of-plane (OOP) magnetic easy axis by fabricating BIG thin films on a GGG(111) substrate. Our results show perpendicular magnetic anisotropy, which can play a crucial role in spintronics and magnonics applications. In this work, we investigate the static and dynamic magnetic properties of BIG films (such as magnetic anisotropies and magnetic damping) and magnetic domain textures using frequency and angular variation of FMR and MFM measurements.

**II. EXPERIMENTAL DETAILS**

A BIG ceramic target was prepared using a solid-state reaction by mixing the constituent oxides, bismuth oxide ( $\text{Bi}_2\text{O}_3$ ; purity  $\geq 99.9\%$ , Aldrich Chemical Company) and iron ox-

\*Present address: DOD Center of Excellence for Advanced Electro-Photonics with 2D Materials, Department of Physics, Morgan State University, Baltimore, Maryland 21251, USA.

<sup>†</sup>Present address: Center for Integrated Nanostructure Physics, Institute for Basic Science, Sungkyunkwan University, Suwon 16419, Republic of Korea.

<sup>‡</sup>zakir@iitk.ac.in

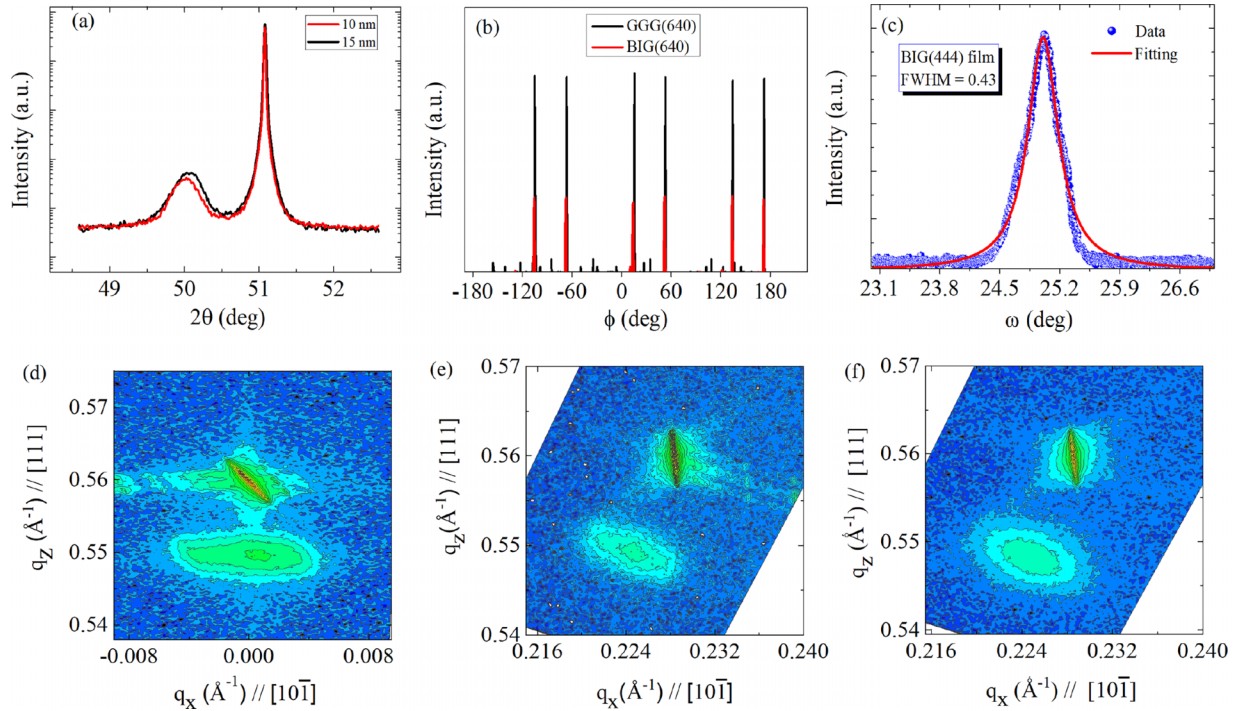


FIG. 1. XRD measurements on BIG/GGG(111) films. (a)  $\theta$ - $2\theta$  scans of epitaxial films 10 nm (red) and 15 nm (black) thick. (b)  $\phi$  scans for BIG(640) and GGG(640) for the 15 nm thick film. (c)  $\omega$  scan for the BIG(444) film plane for the 15 nm thick film. RSM along (d) the symmetric (444) and (e) asymmetric (642) planes for the 15 nm thick film. (f) RSM along the asymmetric (642) plane for the 10 nm thick film.

ide ( $\text{Fe}_2\text{O}_3$ ; purity  $\sim 99.9\%$ , Strem Chemicals), in a proper stoichiometry (3:5). The reactant mixture was ground and annealed at  $400^\circ\text{C}$  and  $500^\circ\text{C}$  for 24 h each. The mixture was pressed into a 2.2 cm diameter pellet by applying a pressure of 50–60 atm and sintered at  $600^\circ\text{C}$  for 24 h. The pellet was crushed and thoroughly ground before final pelletization, which was sintered at  $700^\circ\text{C}$  and  $800^\circ\text{C}$  for 24 h each. We achieved a compact hard ceramic pellet which is mounted inside the pulsed laser deposition (PLD) chamber for BIG thin film deposition on a GGG(111) substrate. The PLD system is equipped with a KrF excimer laser (Lambda Physik COMPex Pro,  $\lambda = 248$  nm). Thin films with thicknesses of 15 and 10 nm were grown at a temperature of  $500^\circ\text{C}$  in the presence of  $4.0 \times 10^{-2}$  mbar  $\text{O}_2$  gas pressure. The laser was fired at a repetition rate of 2 Hz with energy and spot size of 70 mJ and  $8.0$  mm $^2$ , respectively, leading to an energy density of  $0.87$  J/cm $^2$  on the target surface, which was placed 4 cm away from the substrate. The as-grown films were examined with the help of the x-ray diffraction (XRD) technique using a PANalytical X'Pert PRO setup provided with a Cu  $K\alpha_1$  source ( $\lambda = 1.5405$  Å). We performed  $\theta$ - $2\theta$ ,  $\phi$ , and  $\omega$  scans to probe the crystallinity of the grown films. In addition, we performed a  $\sin^2 \psi$  measurement in the XRD setup to quantify the residual stress in the films. The magnetic domain imaging was carried out in ultrahigh vacuum ( $\approx 1.33 \times 10^{-9}$  mbar) at 300 K, using a scanning probe microscope (UHV 3500, RHK Technology) which is equipped with an electromagnet to apply IP magnetic field. All measurements were performed in the noncontact mode using a cobalt-chromium-coated magnetic tip. The static magnetic measurements were carried out using a Quantum Design magnetic property measurement system (MPMS) at room temperature. For the dynamic magnetic

measurements, we used a commercial electron paramagnetic resonance (EPR) spectrometer (Bruker EMX) operating at a fixed cavity frequency of 9.6 GHz and a custom-made broadband FMR spectrometer. A custom-made broadband FMR spectrometer with a  $300$   $\mu\text{m}$  wide coplanar waveguide (CPW) was designed to record FMR spectra at different frequencies. The thin films were mounted on the top of the CPW using the flip-chip technique. The CPW assembly was housed between the pole pieces of an electromagnet. The FMR spectra were recorded by employing field modulation and the lock-in detection technique to enhance the signal-to-noise ratio. The modulation frequency of 1000 Hz and modulation field amplitude of 5 Oe were fixed during the measurement [17,22].

### III. RESULTS AND DISCUSSION

#### A. Structural analysis

In Fig. 1(a), XRD  $\theta$ - $2\theta$  scans for 10 nm (in red) and 15 nm (in black) films show peaks corresponding to BIG(444) and GGG(444). These peaks indicate epitaxial growth of BIG films on GGG(111) substrates, with lattice mismatch  $\Delta a = (a_{\text{film}} - a_{\text{sub}} = 12.609 - 12.380)$  Å =  $0.229$  Å for 15 nm thick film and  $\Delta a = (12.621 - 12.380)$  Å =  $0.241$  Å for 10 nm thick film. XRD  $\phi$  scans for the 15 nm thick BIG film and the substrate in Fig. 1(b) show sixfold symmetry in the (640) plane; the coinciding peaks of the BIG film and GGG substrate further confirm the epitaxial growth. The XRD  $\omega$  scan in Fig. 1(c) was performed on the (444) plane of the 15 nm thick film. The FWHMs of the  $\omega$  scan for both films are almost identical,  $\sim 0.43^\circ$ . The reciprocal space map (RSM) for the 15 nm BIG film is shown in Fig. 1(d) for the symmetric (444) plane and in Fig. 1(e) for the asymmetric (642)

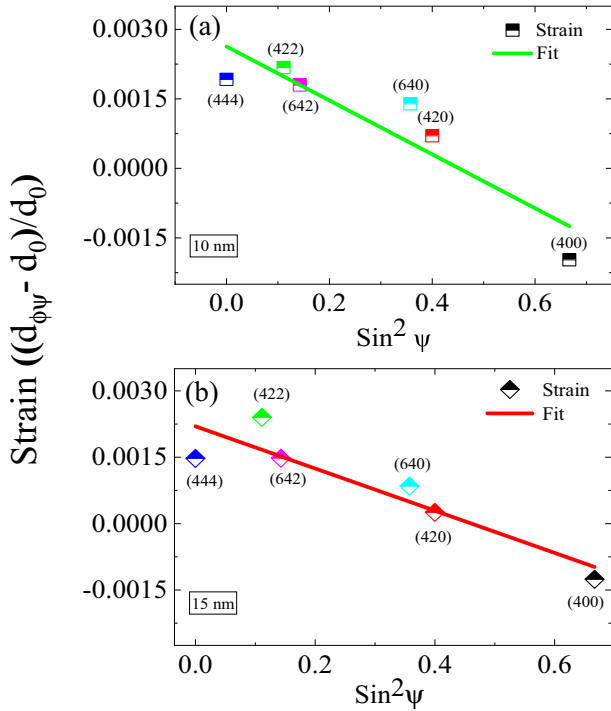


FIG. 2. The  $\sin^2 \psi$  plot for the calculation of the residual stress (a) for 10 and (b) 15 nm thick BIG/GGG(111) films; green and red lines are fits to the experimental data for the 10 nm and 15 nm thick films, respectively.

plane. The RSM shows the single-phase epitaxial growth and exact strain state of the film. Lattice parameters were calculated from the RSM using the formula for IP  $a_{in} = (2\sqrt{2})/q_x$  and for OOP  $a_{out} = (4\sqrt{3})/q_z$ . The lattice parameters for the 15 nm BIG film are  $a_{in}(\text{BIG}) = 12.598 \text{ \AA}$  and  $a_{out}(\text{BIG}) = 12.609 \text{ \AA}$ . Similarly, for the 10 nm thick film, RSM along the (642) plane is shown in Fig. 1(f). The lattice parameters calculated for the 10 nm thick film are  $a_{in}(\text{BIG}) = 12.592 \text{ \AA}$  and  $a_{out}(\text{BIG}) = 12.621 \text{ \AA}$ , and they match literature values well [16,23]. The asymmetric plane (642) RSM shows the film and substrate have different  $q_x$  values, indicating the relaxation of the BIG film on the GGG substrate. This might be due to larger lattice mismatch induced strain getting released through misfit dislocations. Residual stress was calculated using the nondestructive  $\sin^2 \psi$  XRD technique by performing  $\theta$ - $2\theta$  scans in different film planes using  $\psi$  tilt. The strain calculated from the lattice spacing is plotted against  $\sin^2 \psi$  in Fig. 2(a) for the 10 nm thick film and in Fig. 2(b) for the 15 nm thick film, and the fitting was done using the following equation [24]:

$$\epsilon_{\phi\psi} = \frac{d_{\phi\psi} - d_0}{d_0} = \frac{1+\nu}{E} \sigma_{\phi} \sin^2 \psi - \frac{\nu}{E} (\sigma_{11} + \sigma_{22}), \quad (1)$$

$$\sigma_{\phi} = \sigma_{11} \cos^2 \phi + \sigma_{12} \sin 2\phi + \sigma_{22} \sin^2 \phi. \quad (2)$$

Here,  $\epsilon_{\phi\psi}$  is the strain calculated using the value of  $d_0$  representing the relaxed lattice spacing parameter, and  $d_{\phi\psi}$  is the interplanar spacing for the thin film;  $\nu$  and  $E$  are the Poisson ratio and Young's modulus, respectively.  $\sigma_{\phi}$  represents the surface stress along the  $\phi$  direction. The linear fitting in the strain  $\epsilon_{\phi\psi}$  vs  $\sin^2 \psi$  plot (shown in Fig. 2) provides residual

stress values of  $-0.77$  and  $-0.93$  GPa for the 15 and 10 nm thick films, respectively. The negative sign of  $\sigma_{\phi}$  for both films confirms the presence of in-plane compressive stress. We used the reported Poisson's ratio (0.29) and Young's modulus (206 GPa) of the BIG crystal [25,26] for the calculations.

### B. MFM analysis

MFM is a powerful technique to study magnetic domains and offers insight into the magnetization distribution in the sample in terms of high-resolution micro- and nanosized domains. Figure 3 shows MFM images with different values of magnetic field applied in a direction parallel to the film plane. MFM images show magnetic domains with bright and dark contrast. The bright and dark contrast represent domains whose  $\vec{M}$  lies out of and into the film plane, respectively. As the value of the IP magnetic field increases, the domain size with distinct bright and dark contrast starts to decrease, as shown in Figs. 3(a)–3(e). At an applied field of 2265 G, the domains almost disappear. Furthermore, on retracing the applied field in Figs. 3(f)–3(i), the domains with dark and bright contrast reappear. This confirms that the contrast in the MFM images indeed comes from magnetic domains and not from topographic features of the film. The decrease of the domain size followed by the near disappearance of the MFM contrast at higher fields can be explained in terms of the applied IP field aligning  $\vec{M}$  along the film plane. With  $\vec{M}$  in the film plane, it exerts no force on the magnetic tip (magnetized perpendicular to the film plane), and hence, the MFM contrast disappears. This in turn implies  $\vec{M}$  in the BIG/GGG(111) thin film is in a canted state, oriented at some angle with respect to the film plane. We have extracted the canting angle  $\theta$  from the MFM images,  $\theta = \sin^{-1}(\text{MFM}_{\text{Intensity}}/\text{MFM}_{\text{Intensity}_{\text{Max}}})$ , where  $\text{MFM}_{\text{Intensity}}$  is the intensity of the MFM signal and  $\text{MFM}_{\text{Intensity}_{\text{Max}}}$  is the MFM signal with the maximum intensity [18,27]. The  $\theta$  map corresponding to the MFM image for the BIG/GGG(111) film with  $B = 0$  is displayed in Fig. 4. It can be clearly observed that the majority of the domains exhibit  $\vec{M}$  in a canted state, where the canting angle ranges from  $-30^\circ < \theta < +30^\circ$ .

### C. Magnetization and FMR analysis

The magnetization measurements were performed at room temperature using a Quantum Design MPMS. We trace hysteresis loops for both IP and OOP geometry after subtracting the paramagnetic contribution of the GGG(111) substrate, as shown in Fig. 5. For the 15 nm BIG film,  $4\pi M_s$  for both IP and OOP loops look identical. Therefore, we can infer from the hysteresis measurements that the magnetic easy axis is canted at some angle to the film plane. However, the relatively thinner film of thickness 10 nm shows an OOP easy axis. This is further confirmed with FMR analysis. The coercive field  $H_c$  and  $4\pi M_s$  are estimated to be  $\sim 15$  and  $\sim 1068$  Oe, respectively, from the in-plane  $M$ - $H$  loop for the 15 nm thick film. Similarly, for the 10 nm thick film,  $H_c$  and  $4\pi M_s$  are found to be  $\sim 39$  Oe and  $\sim 942$  Oe, respectively.

In order to study static and dynamic magnetic properties, FMR measurements with frequency and angular (IP and OOP) variations were performed. The polar coordinate system used

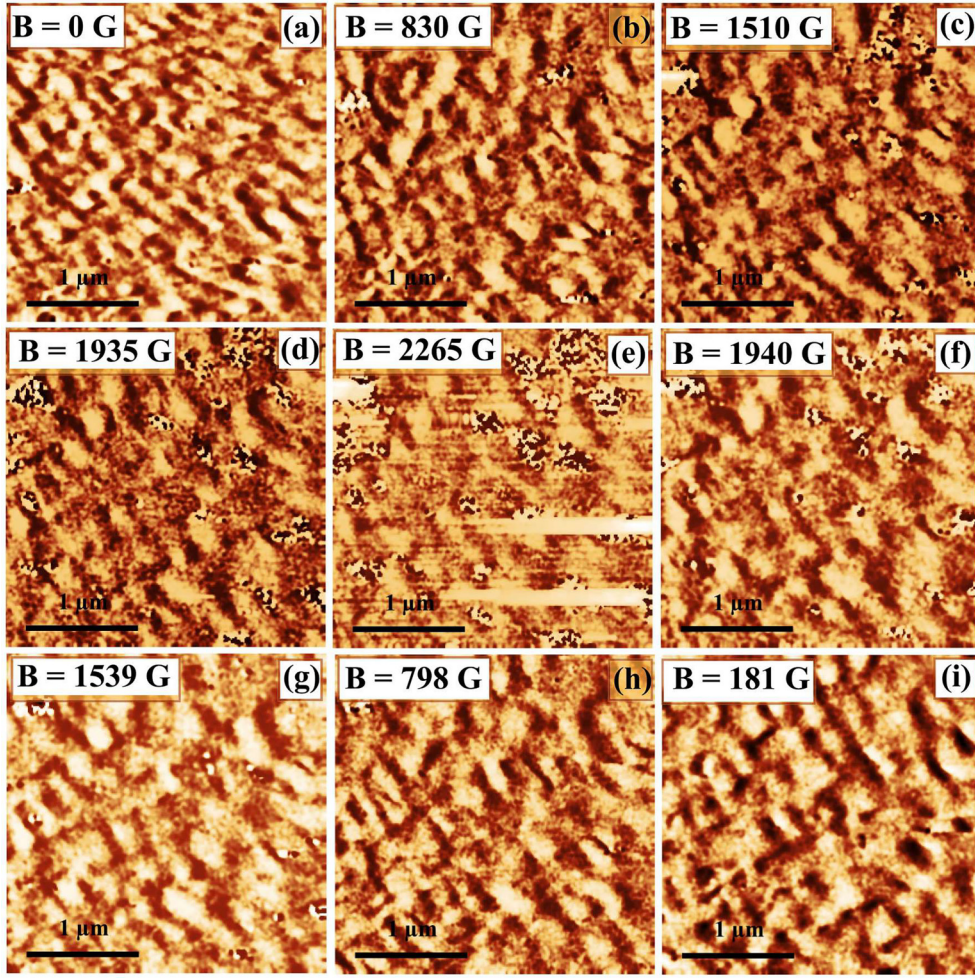


FIG. 3. MFM images of the 15 nm BIG/GGG(111) epitaxial thin film. Images show domain evolution with (a)–(e) increasing and (f)–(i) decreasing IP applied magnetic fields.

in the subsequent discussion of the BIG(111) epitaxial film is illustrated in Fig. 6(a).  $\varphi_H$  ( $\varphi_M$ ) is the IP angle between  $H$  ( $M$ ) and the  $x$  axis, and  $\theta_H$  ( $\theta_M$ ) is the polar angle between  $H$  ( $M$ ) and the  $z$  axis.  $\varphi_6$  denotes the IP sixfold symmetry in the azimuthal direction with respect to the  $x$  axis. The total free energy density  $F$  for (111) oriented cubic garnet magnetic systems can be written as [28,29]

$$\begin{aligned}
 F = & -M_S H \left[ \frac{\sin \theta_H \sin \theta_M \cos(\varphi_H - \varphi_M)}{\cos \theta_H \cos \theta_M} \right] + 2\pi M_S^2 \cos^2 \theta_M + K_{6\parallel} \sin^6 \theta_M \cos 6(\varphi_M - \varphi_6) - K_{1\perp} \cos^2 \theta_M \\
 & - K_{2\perp} \cos^4 \theta_M - K_{6\perp} \cos^6 \theta_M + \frac{K_1}{12} (7\sin^4 \theta_M - 8\sin^2 \theta_M + 4 - 4\sqrt{2}\sin^3 \theta_M \cos \theta_M \cos 3\varphi_M) \\
 & + \frac{K_2}{108} [-24\sin^6 \theta_M + 45\sin^4 \theta_M - 24\sin^2 \theta_M + 4 - 2\sqrt{2}\sin^3 \theta_M \cos \theta_M (5\sin^2 \theta_M - 2) \cos 3\varphi_M + \sin^6 \theta_M \cos 6\varphi_M], \quad (3)
 \end{aligned}$$

where the first two energy terms are contributed by Zeeman and dipolar demagnetizations (shape anisotropy). The third, fourth, fifth, and sixth energy terms correspond to the in-plane sixfold and first-, second-, and sixth-order PMA energies, respectively. The last two terms are the first- and second-order cubic magnetocrystalline anisotropy energies. The respective magnetic anisotropy constants written in a similar fashion are  $K_{6\parallel}$ ,  $K_{1\perp}$ ,  $K_{2\perp}$ ,  $K_{6\perp}$ ,  $K_1$ , and  $K_2$ . Under equilibrium conditions,

the resonance frequency  $f_r$  of the uniform precession mode can be obtained from the total free energy density by using the following expression [30,31]:

$$f_r^2 = \left( \frac{\gamma}{2\pi} \right)^2 \frac{1}{M_S^2 \sin^2 \theta_M} \left[ \frac{\partial^2 F}{\partial \theta_M^2} \frac{\partial^2 F}{\partial \varphi_M^2} - \left( \frac{\partial^2 F}{\partial \theta_M \partial \varphi_M} \right)^2 \right], \quad (4)$$

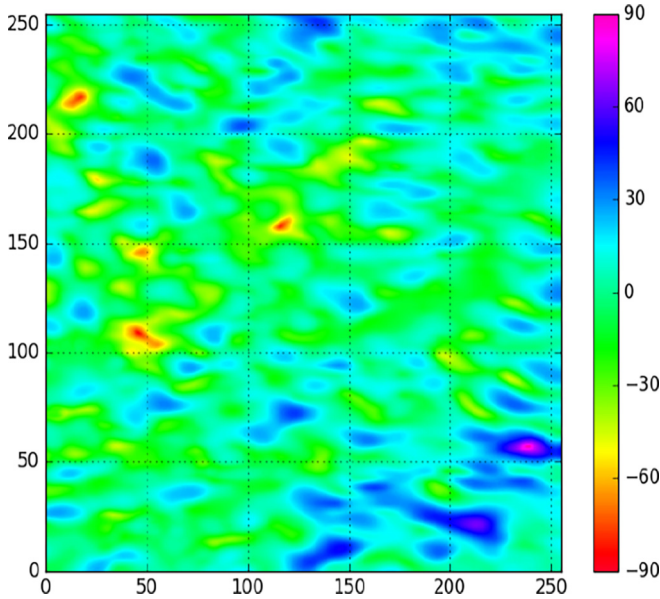


FIG. 4. Map of the canting angle  $\theta$  extracted from the MFM image for  $B = 0$ . Canting of  $M$  can be clearly observed, where  $\theta$  lies in the range  $-30^\circ$  to  $30^\circ$ .  $x$  and  $y$  axes represent the pixels number, while the color bar represents the value of  $\theta$ .

where  $\gamma$  denotes the gyromagnetic ratio, which is related to the Landé  $g$  factor as follows:  $\gamma/2\pi = g \times 1.39 \times 10^6$  Hz/Oe. The equilibrium angles of magnetization  $\varphi_M$  and  $\theta_M$  can be obtained by solving the coupled equations after the energy minimization ( $\partial F/\partial\varphi_M = \partial F/\partial\theta_M = 0$ ) and incorporating the  $H_r$  solution in the resonance frequency expression. The numerical solutions of these coupled and indirectly defined functional equations were determined using *Mathematica*. The  $\varphi_M$  and  $\theta_M$  values for each value of  $\varphi_H$  and  $\theta_H$  were used to fit the IP and OOP angular variations of the resonance field ( $H_r$  vs  $\varphi_H$  and  $H_r$  vs  $\theta_H$ ).

To determine the IP anisotropy constant, in-plane angular variations of FMR spectra were recorded at 9.6 and 10.5 GHz frequencies for the 15 and 10 nm thick BIG films, respectively. The film is rotated about the [111] axis, which is perpendicular to the film plane. Figure 7 shows the  $\varphi_H$  dependence of  $H_r$  of the uniform FMR mode at 9.6 and 10.5 GHz for the 15 and 10 nm thick BIG films, respectively. The 15 nm thick film shows sixfold symmetry and matches the crys-

talline symmetry of BIG. This is in agreement with reported (111) oriented YIG crystals [32–36]. The experimental data points are fitted by solving the coupled equations presented in Eqs. (3) and (4). The sixfold symmetry is introduced in the total free energy density to fit the  $\varphi_H$  dependence of  $H_r$  for the 15 nm thick film. The value of  $K_{6\parallel}$  is found to be  $1.2 \times 10^2$  erg/cm<sup>3</sup> for the 15 nm thick film. However, the 10 nm thick film shows fourfold symmetry with a unidirectional feature. The increase in lattice strain in the 10 nm thick film leads to the evolution of fourfold magnetic anisotropy. The experimental data points are modeled numerically by incorporating the fourfold ( $K_{4\parallel}$ ) and unidirectional ( $K_d$ ) magnetic anisotropies in Eq. (3).  $K_{4\parallel}$  and  $K_d$  are estimated as  $7.5 \times 10^2$  and  $-5.5 \times 10^2$  erg/cm<sup>3</sup>, respectively. The change in IP symmetry from sixfold to fourfold by means of the reduction of the film thickness might be due to the interfacial symmetry breaking and the change in the electronic structure [21]. The typical frequency variation of  $H_r$  along the IP easy axis ( $\varphi_6 = 30^\circ$ ) and hard axis ( $\varphi_6 = 0^\circ$ ) for the 15 nm thick film is shown in Fig. 6(b) as solid circles. The experimental data points are fitted by using Kittel's equation [17]. The effective magnetization ( $4\pi M_{\text{eff}}$ ) can be expressed as  $4\pi M_{\text{eff}} = 4\pi M_S - H_A$ , where  $H_A$  is the effective anisotropy field. From curve fitting, we estimate a value of  $4\pi M_{\text{eff}} = -250$  Oe. The small and negative value of  $4\pi M_{\text{eff}}$  indicates that the magnetic easy axis has switched from IP to OOP. Figure 6(c) shows the frequency dependence of  $H_r$  for the 10 nm thick film at  $\theta_H = 90^\circ$  and  $0^\circ$ . We use Kittel's equation [4] to fit the experimental data points.  $\gamma/2\pi$  and  $4\pi M_{\text{eff}}$  are estimated as  $2.80 \times 10^6$  Hz/Oe and  $-216$  Oe, respectively. The  $g$  factors are estimated to be 1.96 and 2.00 for the 15 and 10 nm thick films, respectively. The  $g$  factors are close to the spin-only value of the electron.

The polar angle  $\theta_H$  variations of FMR spectra were recorded at frequencies of 9.6 and 10.5 GHz for the 15 and 10 nm thick films, respectively. The plots of  $H_r$  vs  $\theta_H$  are shown in Fig. 8. For the 15 nm thick film the value of  $H_r$  is found to be the minimum at  $\theta_H = 65^\circ$ . This shows that the magnetic easy axis lies OOP and makes an angle of  $\theta = 90^\circ - 65^\circ = 25^\circ$  with respect to the film plane. This value of  $25^\circ$  corroborates our earlier MFM result, which indicated canting angle in the range of  $-30^\circ$  to  $30^\circ$ . A similar variation of  $H_r$  was observed in the CoFeB/MgO structure with an oblique magnetic easy axis [37,38]. The difference in  $H_r$  values at  $\theta_H = 0^\circ$  and  $\theta_H = 90^\circ$  was observed to be 50 Oe. Such a low difference value for  $H_r$  suggests that the shape-induced demagnetization field is suppressed by the induced PMA. The parameters obtained from the numerical fitting are  $K_{1\perp} = 3.80 \times 10^4$  erg/cm<sup>3</sup>,  $K_{2\perp} = 1.5 \times 10^3$  erg/cm<sup>3</sup>,  $K_{6\perp} = 4.50 \times 10^2$  erg/cm<sup>3</sup>,  $K_1 = 7.0 \times 10^3$  erg/cm<sup>3</sup>,  $K_2 = -5.9 \times 10^3$  erg/cm<sup>3</sup>, and  $H_A = 1054$  Oe. The estimated parameters provide the value of the net anisotropy field, which has a magnitude comparable to that of the demagnetizing field. The relatively smaller thickness of the 10 nm thick film clearly shows the magnetic easy axis perpendicular to the film plane. The reorientation of the easy axis is due to the dominant PMA over the shape anisotropy. The parameters obtained from the numerical fitting are  $K_{1\perp} = 4.20 \times 10^4$  erg/cm<sup>3</sup>,

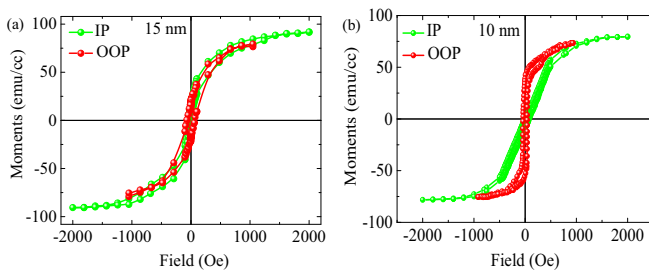


FIG. 5.  $M$ - $H$  loops of BIG/GGG(111) (a) 15 and (b) 10 nm thick films, measured for the in-plane (IP) and out-of-plane (OOP) configurations at room temperature.

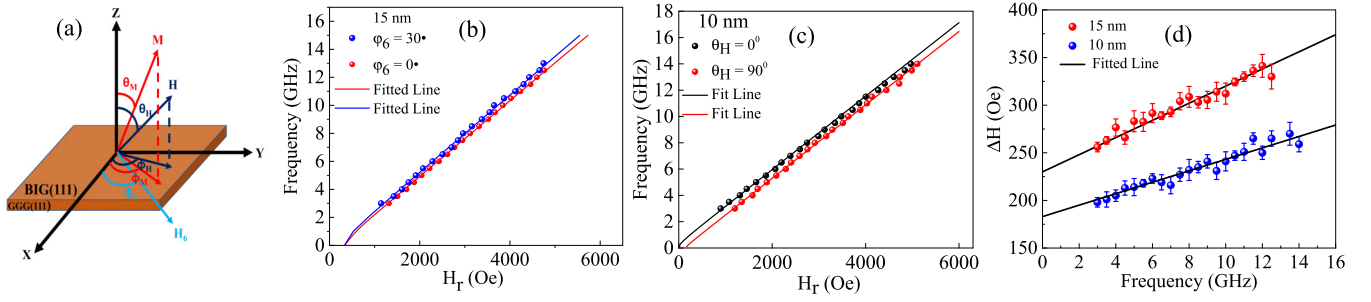


FIG. 6. (a) Geometry for the FMR measurement.  $\vec{H}$  and  $\vec{M}$  represent the direction of applied magnetic field and resultant magnetization. (b) and (c) In-plane  $f$  vs  $H_r$  for 15 and 10 nm thick films, respectively. (d) In-plane frequency variation of the FMR linewidth for the 15 and 10 nm thick films. The solid lines represent the fit to the experimental data.

$K_{4\perp} = 1.00 \times 10^2$  erg/cm<sup>3</sup>,  $K_1 = 3.0 \times 10^3$  erg/cm<sup>3</sup>,  $K_2 = -1.5 \times 10^3$  erg/cm<sup>3</sup>, and  $H_A = 1211$  Oe. The positive sign of  $K_{1\perp}$  signifies that  $\vec{M}$  is out of plane, which is in good agreement with other reported BIG films exhibiting PMA [39].

The effective magnetic anisotropy  $K_{\text{eff}}$  is composed of cubic magnetocrystalline anisotropies ( $K_1$  and  $K_2$ ), magnetoelastic anisotropy ( $K_\sigma$ ), and shape anisotropy ( $K_{\text{shape}}$ ) and can be written as [12]

$$K_{\text{eff}} = K_1 + K_2 + K_\sigma + K_{\text{shape}}, \quad (5)$$

$$K_\sigma = -\frac{3}{2} \frac{E}{1 + \nu} \lambda_{111} \frac{a_{\text{sub}} - a_{\text{film}}}{a_{\text{film}}}, \quad (6)$$

$$K_{\text{shape}} = 2\pi M_S^2. \quad (7)$$

The formulation of all the anisotropies is defined relative to the  $z$  axis (normal to the film plane).  $K_\sigma$  is the magnetoelastic anisotropy, which arises due to the induced strain in epitaxial films.  $E$ ,  $\nu$ , and  $\lambda_{111}$  denote Young's modulus, Poisson's ratio, and the magnetostriction constant in the [111] direction, respectively.  $a_{\text{film}}$  and  $a_{\text{sub}}$  are defined as lattice parameters for the film and substrate, respectively.  $(a_{\text{sub}} - a_{\text{film}})/a_{\text{film}}$  is the induced strain  $\epsilon_{\parallel}$  along the [111] direction.  $K_\sigma$  tries to reorient  $\vec{M}$  along the perpendicular direction depending on

the sign of  $\lambda_{111}$  and  $\epsilon_{\parallel}$ . In order to estimate  $K_\sigma$  in our BIG film, we have used the values  $E = 206$  GPa,  $\nu = 0.29$ , and  $\lambda_{111} = -4.61 \times 10^{-6}$  reported earlier for BIG [25,26]. The negative sign of  $K_\sigma$  is consistent with the out-of-plane magnetic easy axis and is in good agreement with other reported REIGs [12,13,40,41].  $K_{\text{shape}}$  is well known in magnetic thin films which depend on the geometry and  $M_S$ .  $K_{\text{eff}}$  value for the 15 nm thick film was estimated to be  $-1.51 \times 10^5$  erg/cm<sup>3</sup>. Similarly,  $K_{\text{eff}}$  for the 10 nm thick film is estimated to be  $-1.71 \times 10^5$  erg/cm<sup>3</sup>. The higher negative  $K_{\text{eff}}$  value for the 10 nm thick film is due to the larger exerted strain compared to that of the 15 nm thick film. It has been reported that REIG films with a negative value of  $K_{\text{eff}}$  exhibit PMA [12,13]. The variation of the magnetic easy axis can be visualized through the energy surface plot shown in Fig. 9, where  $K_{1\perp}$  varies from  $-1.0 \times 10^5$  to  $1.0 \times 10^5$  in the  $H_r$  vs  $\theta_H$  plot. A higher magnitude of  $K_{1\perp}$  with a negative sign and a positive sign indicates that the easy axis of  $\vec{M}$  is oriented along the film plane and perpendicular to the film plane, respectively.

Magnetic relaxation was investigated by measuring the frequency dependence of the linewidth  $\Delta H$  for the IP configuration of the 15 and 10 nm thick films, as shown in Fig. 6(d). The magnetic damping has two different origins: (i) Gilbert-type relaxation and (ii) non-Gilbert-type relaxation. The former arises due to direct transfer of energy from the

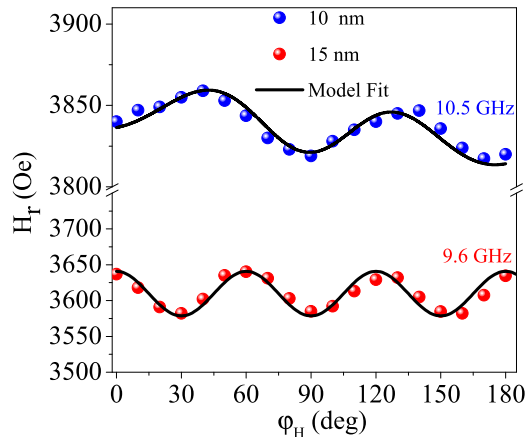


FIG. 7. In-plane angular  $\phi_H$  variation of  $H_r$ . Solid red (15 nm) and blue (10 nm) dots are the experimental data points, while the black solid line represents the model fit.

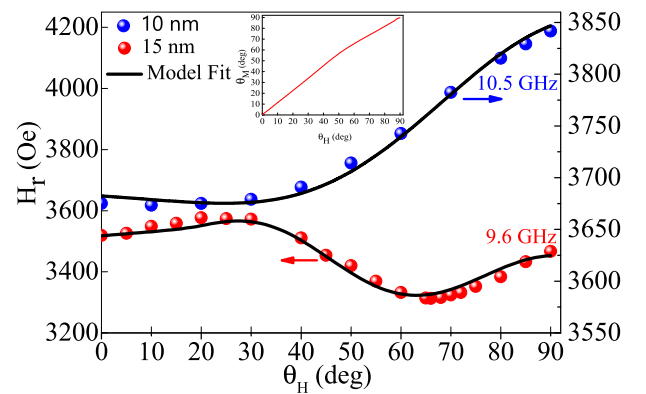


FIG. 8. Out-of-plane angular  $\theta_H$  variation of  $H_r$ . Solid red (15 nm) and blue (10 nm) dots are the experimental data points, while the black solid line represents the model fit. The inset shows the plot of  $\theta_M$  vs  $\theta_H$  for the 15 nm thick BIG film.

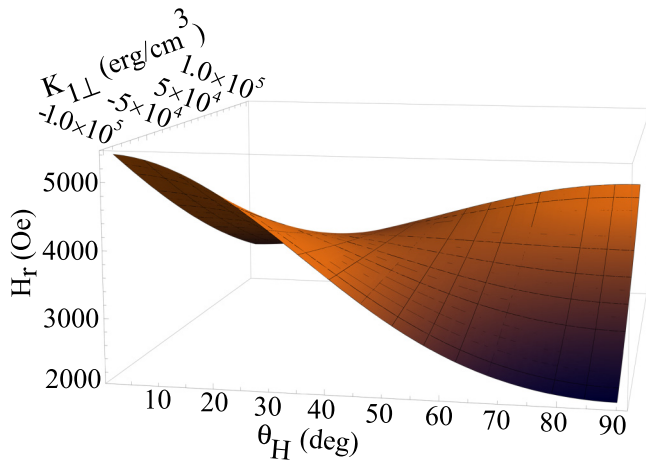


FIG. 9. Energy surface plot: the variation of the magnetic easy axis with different perpendicular magnetic anisotropy constants at 9.6 GHz frequency.

excited spin wave states to the lattice and is considered to be intrinsic damping, whereas the latter is extrinsic damping that arises due to inhomogeneities. As a result, the local FMR signals for different regions of the film have slightly different magnetic properties and result in linewidth broadening. The intrinsic Gilbert damping coefficient can be estimated using the Landau-Lifshitz-Gilbert equation expressed as [17,42]

$$\Delta H = \Delta H_0 + \frac{2}{\sqrt{3}} \frac{2\pi\alpha}{\gamma} f, \quad (8)$$

where the first term is due to magnetic inhomogeneities and the second term corresponds to Gilbert damping. The parameters  $\Delta H_0 = 230$  Oe and  $\alpha = 2.3 \pm 0.5 \times 10^{-2}$  were estimated from the linear fitting for the 15 nm thick film. Similarly, for the 10 nm thick film, the parameters obtained are  $\Delta H_0 = 183$  Oe and  $\alpha = 1.4 \pm 0.4 \times 10^{-2}$ .  $\alpha$  is comparable to that of bismuth substituted thulium iron garnet (TmBiIG) [40] and  $Y_{3-x}Bi_xFe_5O_{12}$  (BiYIG) with  $x = 0.25$  [17] and relatively lower than that of BiYIG with  $x = 0.92$  [43]. There is large uncertainty in the evaluation of  $\alpha$  values due to the broadening in the linewidth and relatively smaller  $4\pi M_s$ . The  $\alpha$  value is found to be two orders of magnitude higher than that of a YIG film [1,44]. This might be because of the larger lattice mismatch [45] in BIG/GGG(111) in comparison to YIG/GGG(111) and the presence of Bi ions with strong spin-orbit coupling [17,46,47]. REIGs with nonzero  $4f$  moments can possess oxidation states other than  $Re^{3+}$ , i.e.,  $Re^{2+}$  and/or  $Re^{4+}$ , which can enhance the damping due to the nonzero magnetic moment of rare earth ions [48].  $Bi^{3+}$  is not associated with such a case because it has a completely filled  $4f$  ( $4f^{14}$ ) orbital in its electronic configuration.

REIGs have a wide range of magnetostriction coefficients [36] at room temperature, which enables the tuning of magnetic anisotropy in thin films with variable growth parameters, lattice mismatch, and partial or complete substitutions at the rare earth ion sites. The PLD grown unstrained REIG thin films show that the magnetization direction mostly lies in the film plane due to the dominance of shape anisotropy over magnetocrystalline anisotropy. However, with proper

engineering of strain by means of lattice mismatch using suitable substrate and growth parameters, PMA can be achieved in REIG films. The strain may induce PMA at the cost of increased magnetic inhomogeneity and damping factors. We observed the OOP magnetic easy axis in PLD grown epitaxial BIG thin films. For the 15 nm BIG film, the  $M$ - $H$  loops in the IP and OOP orientation have nearly the same saturation field. Such features arise due to the partial compensation of the demagnetizing field (or shape anisotropy) with cubic magnetocrystalline anisotropy and magnetoelastic anisotropy. We observed cubic magnetocrystalline anisotropies ( $K_1$  and  $K_2$ ) and magnetoelastic anisotropy ( $K_\sigma < 0$ ) overcome shape anisotropy,  $|K_1 + K_2 + K_\sigma| > K_{\text{shape}}$ , which results in  $K_{\text{eff}} < 0$  and leads to the OOP magnetic easy axis. Interestingly, the complete IP to OOP reorientation took place in the 10 nm thick BIG film. This reorientation is a result of the increase in lattice strain with decreasing thickness and a subsequent increase in the negative value of  $K_{\text{eff}}$ . A similar observation was reported by Ortiz *et al.*, in which a europium iron garnet (EuIG) film showed IP to OOP reorientation below 56 nm [49]. Systematic variation of strain from a compressive ( $-0.42\%$ ) to tensile ( $0.34\%$ ) regime in EuIG films leads to linear and quadratic dependence of first- and second-order perpendicular magnetic anisotropies, respectively [36]. Tuning of a magnetocrystalline anisotropy field of 1000 Oe using a wide range of strain was reported by Wang *et al.* [50]. The stress-induced anisotropy field of 25 kOe leads to the development of PMA in epitaxial  $Tm_3Fe_5O_{12}$  thin films due to the large negative value of  $\lambda$  which overcomes the shape anisotropy [51]. Strain-induced PMA has been demonstrated in various REIGs [48,52–54]. The negative  $\lambda_{111}$  with the negative strain state enables the film to possess an OOP magnetic easy axis [41]. Since all REIGs except  $Tb_3Fe_5O_{12}$  (TbIG) exhibit negative  $\lambda_{111}$  at room temperature, the tensile or compressive strain determines the sign of the induced anisotropy to be negative or positive and hence the sign of  $K_{\text{eff}}$ . The ionic radii of  $Bi^{3+}$  and  $Y^{3+}$  are 1.03 and 0.9 Å, respectively. The complete replacement of  $Y^{3+}$  ion by  $Bi^{3+}$  ion leads to expansion of the lattice parameter in BIG films (12.609 Å) compared to YIG films (12.376 Å). The deposition of BIG with larger lattice parameters on top of a GGG(111) substrate induces IP compressive strain in the BIG film. It was reported that IP compressive strain with negative  $\lambda_{111}$  leads to the evolution of PMA in HoIG, SmIG, and YIG [13,55]. An in-plane magnetic easy axis was reported for BIG/GGG(001) [19–21], whereas we observed an OOP magnetic easy axis in both the 15 and 10 nm thick films of BIG/GGG(111). The BIG(444) film reflection in Fig. 1(c) shows a broadened XRD peak with a FWHM of  $0.43^\circ$ , indicating a larger strain in BIG/GGG(111) compared to that reported for BIG/GGG(001) with a FWHM of  $0.03^\circ$  [20]. There are reports of EuIG showing PMA [49,51,56–58] with larger lattice mismatch and compressive strain. The nonuniform strain relaxation and magnetic inhomogeneity lead to higher values of  $\Delta H_0$  [36]. This might also be the reason for a higher value of  $\Delta H_0$  along with the high spin-orbit coupling caused by Bi ions in BIG films. The realization of PMA in BIG films can be attributed to the decreasing shape anisotropy and the increase in magnetoelastic and magnetocrystalline anisotropy. BIG films with PMA and other features like higher Faraday rotation and electrical

control of magnetization may draw significant interest in the fields of spintronics and photomagnonics.

#### IV. CONCLUSIONS

We deposited single-phase epitaxial BIG/GGG(111) films to explore the possibility of PMA with angle-dependent FMR measurements and magnetic domain texture. XRD confirmed epitaxial growth of the films. For the 15 nm thick sample, BIG/GGG(111) contains OOP magnetic anisotropy, inferred from the  $M$ - $H$  loop measurements. The  $\theta$ -mapping plot extracted using the MFM images for  $B = 0$  further support the oblique magnetic easy axis, with the canting angle lying in the range  $-30^\circ$  to  $+30^\circ$  with respect to the film plane. For the 10 nm thick film, the magnetic easy axis lies perpendicular

to the film plane. The presence of a Bi ion and IP compressive strain leads to PMA in the BIG films. There is an increase in the damping factor, but still, the Gilbert damping parameters for our BIG film are comparable to reported garnets with PMA. BIG films are known for their microwave application due to higher Faraday rotation. The observed PMA and Gilbert damping in BIG films are promising for spintronic and photomagnonic devices.

#### ACKNOWLEDGMENTS

We gratefully acknowledge the research support from IIT Kanpur and DST, Government of India [Sanction Order No. DST/NM/TUE/QM-06/2019(G)]. The authors thank V. Singh and Dr. A. Kumar Medda for their help with the angle-dependent EPR measurements.

- 
- [1] C. Hauser, T. Richter, N. Homonnay, C. Eisenschmidt, M. Qaid, H. Deniz, D. Hesse, M. Sawicki, S. G. Ebbinghaus, and G. Schmidt, *Sci. Rep.* **6**, 20827 (2016).
- [2] P. Cao Van, S. Surabhi, V. Dongquoc, R. Kuchi, S.-G. Yoon, and J.-R. Jeong, *Appl. Surf. Sci.* **435**, 377 (2018).
- [3] R. Kumar, S. N. Sarangi, D. Samal, and Z. Hossain, *Phys. Rev. B* **103**, 064421 (2021).
- [4] R. Kumar, B. Samantaray, S. Das, K. Lal, D. Samal, and Z. Hossain, *Phys. Rev. B* **106**, 054405 (2022).
- [5] T. Boudiar, B. Payet-Gervy, M.-F. Blanc-Mignon, J.-J. Rousseau, M. Le Berre, and H. Joisten, *J. Magn. Magn. Mater.* **284**, 77 (2004).
- [6] H. Chang, P. Li, W. Zhang, T. Liu, A. Hoffmann, L. Deng, and M. Wu, *IEEE Magn. Lett.* **5**, 1 (2014).
- [7] C. O. Avci, A. Quindeau, C.-F. Pai, M. Mann, L. Caretta, A. S. Tang, M. C. Onbasli, C. A. Ross, and G. S. D. Beach, *Nat. Mater.* **16**, 309 (2017).
- [8] K. Ganzhorn, J. Barker, R. Schlitz, B. A. Piot, K. Ollefs, F. Guillou, F. Wilhelm, A. Rogalev, M. Opel, M. Althammer, S. Geprägs, H. Huebl, R. Gross, G. E. W. Bauer, and S. T. B. Goennenwein, *Phys. Rev. B* **94**, 094401 (2016).
- [9] Q. Shao, Y. Liu, G. Yu, S. K. Kim, X. Che, C. Tang, Q. L. He, Y. Tserkovnyak, J. Shi, and K. L. Wang, *Nat. Electron.* **2**, 182 (2019).
- [10] M. Haertinger, C. H. Back, J. Lotze, M. Weiler, S. Geprägs, H. Huebl, S. T. B. Goennenwein, and G. Woltersdorf, *Phys. Rev. B* **92**, 054437 (2015).
- [11] X.-G. Wang, Z.-X. Li, Z.-W. Zhou, Y.-Z. Nie, Q.-L. Xia, Z.-M. Zeng, L. Chotorlishvili, J. Berakdar, and G.-H. Guo, *Phys. Rev. B* **95**, 020414(R) (2017).
- [12] J. Fu, M. Hua, X. Wen, M. Xue, S. Ding, M. Wang, P. Yu, S. Liu, J. Han, C. Wang, H. Du, Y. Yang, and J. Yang, *Appl. Phys. Lett.* **110**, 202403 (2017).
- [13] S. M. Zanjani and M. C. Onbasli, *AIP Adv.* **9**, 035024 (2019).
- [14] E. Lage, L. Beran, A. U. Quindeau, L. Ohnoutek, M. Kucera, R. Antos, S. R. Sani, G. F. Dionne, M. Veis, and C. A. Ross, *APL Mater.* **5**, 036104 (2017).
- [15] L. Soumah, N. Beaulieu, L. Qassym, C. Carrétéro, E. Jacquet, R. Lebourgeois, J. Ben Youssef, P. Bortolotti, V. Cros, and A. Anane, *Nat. Commun.* **9**, 3355 (2018).
- [16] M.-Y. Chern and J.-S. Liaw, *Jpn. J. Appl. Phys.* **36**, 1049 (1997).
- [17] R. Kumar, B. Samantaray, and Z. Hossain, *J. Phys.: Condens. Matter* **31**, 435802 (2019).
- [18] P. Ghising, Z. Hossain, and R. C. Budhani, *Appl. Phys. Lett.* **110**, 012406 (2017).
- [19] E. Popova, L. Magdenko, H. Niedoba, M. Deb, B. Dagens, B. Berini, M. Vanwolleghem, C. Vilar, F. Gendron, A. Fouchet, J. Scola, Y. Dumont, M. Guyot, and N. Keller, *J. Appl. Phys.* **112**, 093910 (2012).
- [20] E. Popova, A. F. F. Galeano, M. Deb, B. Warot-Fonrose, H. Kachkachi, F. Gendron, F. Ott, B. Berini, and N. Keller, *J. Magn. Magn. Mater.* **335**, 139 (2013).
- [21] E. Popova, A. Shengelaya, D. Daraselia, D. Japaridze, S. Cherifi-Hertel, L. Bocher, A. Gloter, O. Stéphan, Y. Dumont, and N. Keller, *Appl. Phys. Lett.* **110**, 142404 (2017).
- [22] P. Ghising, B. Samantaray, and Z. Hossain, *Phys. Rev. B* **101**, 024408 (2020).
- [23] S. Kahl, S. Khartsev, A. M. Grishin, K. Kawano, G. Kong, R. Chakalov, and J. Abell, *J. Appl. Phys.* **91**, 9556 (2002).
- [24] R. Kumar, Z. Hossain, and R. C. Budhani, *J. Appl. Phys.* **121**, 113901 (2017).
- [25] T. Okuda, T. Katayama, H. Kobayashi, N. Kobayashi, K. Satoh, and H. Yamamoto, *J. Appl. Phys.* **67**, 4944 (1990).
- [26] S. Mino, M. Matsuoka, A. Tate, A. Shibukawa, and K. Ono, *Jpn. J. Appl. Phys.* **31**, 1786 (1992).
- [27] G. Singh, P. Rout, R. Porwal, and R. Budhani, *Appl. Phys. Lett.* **101**, 022411 (2012).
- [28] S. Lee, S. Grudichak, J. Sklenar, C. C. Tsai, M. Jang, Q. Yang, H. Zhang, and J. B. Ketterson, *J. Appl. Phys.* **120**, 033905 (2016).
- [29] L. D. Landau and E. M. Lifshitz, *Electrodynamics of Continuous Media*, 2nd ed. (Pergamon Press, Oxford, 1984).
- [30] H. Suhl, *Phys. Rev.* **97**, 555 (1955).
- [31] J. Smit, *Philips Res. Rep.* **10**, 113 (1955).
- [32] A. Bonda, S. Uba, and L. Uba, *Acta Phys. Pol. A* **121**, 1225 (2012).
- [33] A. Kehlberger, K. Richter, M. C. Onbasli, G. Jakob, D. H. Kim, T. Goto, C. A. Ross, G. Götz, G. Reiss, T. Kuschel, and M. Kläui, *Phys. Rev. Appl.* **4**, 014008 (2015).
- [34] M. C. Onbasli, L. Beran, M. Zahradník, M. Kučera, R. Antoš, J. Mistrík, G. F. Dionne, M. Veis, and C. A. Ross, *Sci. Rep.* **6**, 23640 (2016).



- [35] C. Dubs, O. Surzhenko, R. Linke, A. Danilewsky, U. Brückner, and J. Dellith, *J. Phys. D* **50**, 204005 (2017).
- [36] V. H. Ortiz, B. Arkook, J. Li, M. Aldosary, M. Biggerstaff, W. Yuan, C. Warren, Y. Kodera, J. E. Garay, I. Barsukov, and J. Shi, *Phys. Rev. Mater.* **5**, 124414 (2021).
- [37] A. Okada, S. Kanai, M. Yamanouchi, S. Ikeda, F. Matsukura, and H. Ohno, *Appl. Phys. Lett.* **105**, 052415 (2014).
- [38] G. Yu, Z. Wang, M. Abolfath-Beygi, C. He, X. Li, K. L. Wong, P. Nordeen, H. Wu, G. P. Carman, X. Han, I. A. Alhomoudi, P. K. Amiri, and K. L. Wang, *Appl. Phys. Lett.* **106**, 072402 (2015).
- [39] V. Denysenkov, A. Jalali-Roudsar, N. Adachi, S. Khartsev, A. Grishin, and T. Okuda, *MRS Proc.* **603**, 107 (1999).
- [40] Y. Zhang, Q. Yang, X. Liu, D. Zhang, Y. Rao, and H. Zhang, *AIP Adv.* **11**, 065113 (2021).
- [41] S. Mokarian Zanjani and M. C. Onbaşlı, *J. Magn. Magn. Mater.* **499**, 166108 (2020).
- [42] H. Chang, P. A. P. Janantha, J. Ding, T. Liu, K. Cline, J. N. Gelfand, W. Li, M. C. Marconi, and M. Wu, *Sci. Adv.* **3**, e1601614 (2017).
- [43] G. G. Siu, C. M. Lee, and Y. Liu, *Phys. Rev. B* **64**, 094421 (2001).
- [44] C. Hahn, G. de Loubens, O. Klein, M. Viret, V. V. Naletov, and J. Ben Youssef, *Phys. Rev. B* **87**, 174417 (2013).
- [45] A. Krysztofik, S. Özoğlu, R. D. McMichael, and E. Coy, *Sci. Rep.* **11**, 14011 (2021).
- [46] J. Yang, Y. Xu, F. Zhang, and M. Guillot, *J. Phys.: Condens. Matter* **18**, 9287 (2006).
- [47] E. Jesenska, T. Yoshida, K. Shinozaki, T. Ishibashi, L. Beran, M. Zahradnik, R. Antos, M. Kučera, and M. Veis, *Opt. Mater. Express* **6**, 1986 (2016).
- [48] C. Tang, P. Sellappan, Y. Liu, Y. Xu, J. E. Garay, and J. Shi, *Phys. Rev. B* **94**, 140403(R) (2016).
- [49] V. H. Ortiz, M. Aldosary, J. Li, Y. Xu, M. I. Lohmann, P. Sellappan, Y. Kodera, J. E. Garay, and J. Shi, *APL Mater.* **6**, 121113 (2018).
- [50] H. Wang, C. Du, P. C. Hammel, and F. Yang, *Phys. Rev. B* **89**, 134404 (2014).
- [51] M. Kubota, A. Tsukazaki, F. Kagawa, K. Shibuya, Y. Tokunaga, M. Kawasaki, and Y. Tokura, *Appl. Phys. Express* **5**, 103002 (2012).
- [52] A. Quindeau, C. O. Avci, W. Liu, C. Sun, M. Mann, A. S. Tang, M. C. Onbasli, D. Bono, P. M. Voyles, Y. Xu, J. Robinson, G. S. D. Beach, and C. A. Ross, *Adv. Electron. Mater.* **3**, 1600376 (2017).
- [53] Y. Liu, H. Wong, K. Lam, K. Chan, C. Mak, and C. Leung, *J. Magn. Magn. Mater.* **468**, 235 (2018).
- [54] Q. Shao, A. Grutter, Y. Liu, G. Yu, C.-Y. Yang, D. A. Gilbert, E. Arenholz, P. Shafer, X. Che, C. Tang, M. Aldosary, A. Navabi, Q. L. He, B. J. Kirby, J. Shi, and K. L. Wang, *Phys. Rev. B* **99**, 104401 (2019).
- [55] Z. Capku, C. Deger, P. Aksu, and F. Yildiz, *IEEE Trans. Magn.* **56**, 1 (2020).
- [56] C. Warren, V. Ortiz, L. Scipioni, J. Greer, J. Shi, Y. Kodera, and J. Garay, *J. Magn. Magn. Mater.* **560**, 169513 (2022).
- [57] E. R. Rosenberg, L. Beran, C. O. Avci, C. Zeledon, B. Song, C. Gonzalez-Fuentes, J. Mendil, P. Gambardella, M. Veis, C. Garcia, G. S. D. Beach, and C. A. Ross, *Phys. Rev. Mater.* **2**, 094405 (2018).
- [58] M. X. Guo, C. K. Cheng, Y. C. Liu, C. N. Wu, W. N. Chen, T. Y. Chen, C. T. Wu, C. H. Hsu, S. Q. Zhou, C. F. Chang, L. H. Tjeng, S. F. Lee, C. F. Pai, M. Hong, and J. Kwo, *Phys. Rev. Mater.* **6**, 054412 (2022).